Lake-Effect Snowbands in Baroclinic Environments

DANIEL T. EIPPER, STEVEN J. GREYBUSH, GEORGE S. YOUNG, AND SETH SASLO

Department of Meteorology and Atmospheric Science, The Pennsylvania State University, University Park, Pennsylvania

TODD D. SIKORA AND RICHARD D. CLARK

Department of Earth Sciences, Millersville University, Millersville, Pennsylvania

(Manuscript received 20 November 2018, in final form 22 August 2019)

ABSTRACT

Lake-effect snowstorms are often observed to manifest as dominant bands, commonly produce heavy localized snowfall, and may extend large distances inland, resulting in hazards and high societal impact. Some studies of dominant bands have documented concomitant environmental baroclinity (i.e., baroclinity occurring at a scale larger than the width of the parent lake), but the interaction of this baroclinity with the inland structure of dominant bands has been largely unexplored. In this study, the thermodynamic environment and thermodynamic and kinematic structure of simulated dominant bands are examined using WRF reanalyses at 3-km horizontal resolution and an innovative technique for selecting the most representative member from the WRF ensemble. Three reanalysis periods are selected from the Ontario Winter Lake-effect Systems (OWLeS) field campaign, encompassing 185 simulation hours, including 155 h in which dominant bands are identified. Environmental baroclinity is commonly observed during dominant-band periods and occurs in both the north–south and east–west directions. Sources of this baroclinity are identified and discussed. In addition, case studies are conducted for simulation hours featuring weak and strong along-band environmental baroclinity, resulting in weak and strong inland extent, respectively. These contrasting cases offer insight into one mechanism by which along-band environmental baroclinity can influence the inland structure and intensity of dominant bands: in the case with strong environmental baroclinity, inland portions of this band formed under weak instability and therefore exhibit slow overturning, enabling advection far inland under strong winds, whereas the nearshore portion forms under strong instability, and the enhanced overturning eventually leads to the demise of the inland portion of the band.

1. Introduction

Lake-effect snowstorms have been studied for many years because of their large impact on society (e.g., Jiusto and Kaplan 1972; Niziol et al. 1995; Kristovich et al. 2017; Villani et al. 2017). Some of these studies, including several recent ones, have documented the presence of baroclinity occurring at a scale larger than the width of the parent lake, which is here referred to as environmental baroclinity (e.g., Passarelli and Braham 1981; Campbell and Steenburgh 2017; Steenburgh and Campbell 2017; Eipper et al. 2018). In particular, Eipper et al. (2018) found that cold air advection (CAA) in the upper portion of the boundary layer (BL) was strongly correlated with the inland penetration of lake-effect radar echoes. However, the influence of environmental baroclinity on the far-inland kinematic and dynamic structure of lake-effect snowbands has received little attention. Here we extend the investigation of Eipper et al. (2018) by evaluating environmental baroclinity in lake-effect settings and exploring the influences of both weak and strong environmental baroclinity on the inland structure of lake-effect snowbands.

Lake-effect snowstorms are known to form in diverse modes or morphologies, including 1) multiple wind-parallel rolls (cloud streets; e.g., Sikora et al. 2001), 2) mesoscale vortices, and 3) one or sometimes two band(s) parallel to the major axis of an elongated body of water (e.g., Holroyd 1971; Kelly 1986; Hjelmfelt 1990; Kristovich and Steve 1995; Niziol et al. 1995). This last category of snowstorms, referred to as *enlarged lake storms* by Holroyd (1971) and *shoreline bands*

Corresponding author: Steven J. Greybush, sjg213@psu.edu

DOI: 10.1175/WAF-D-18-0191.1

© 2019 American Meteorological Society. For information regarding reuse of this content and general copyright information, consult the AMS Copyright Policy (www.ametsoc.org/PUBSReuseLicenses).

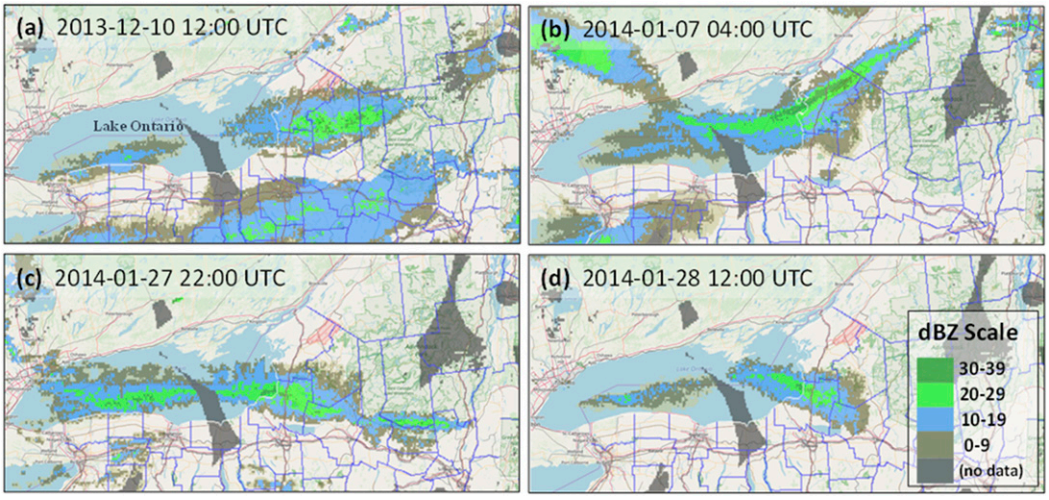

FIG. 1. (a)–(d) Images of NEXRAD equivalent radar reflectivity factor (reflectivity; dBZ); images are 4000-ft constant-altitude plan position indicator (CAPPI) displays (see section 2). Each panel features a dominant band extending inland from Lake Ontario. Note that (a) presents an LLAP band (and hence a shoreline$_{LWK}$ band), but (b), (c), and (d) exhibit departures from the classic LLAP-band morphology (e.g., bends in the band and segments of the band oriented at an oblique angle to the major axis of Lake Ontario). See text for further discussion on the dominant band classification.

by Laird et al. (2003; hereafter shoreline$_{LWK}$ bands) has received much attention in the literature, due to the intense, localized snowfall, and high human impact frequently associated with these storms (e.g., Peace and Sykes 1966; Ballentine 1982; Byrd et al. 1991; Niziol et al. 1995; Steiger et al. 2013; Minder et al. 2015; Veals and Steenburgh 2015; Campbell et al. 2016; Villani et al. 2017). The presence of an appreciable along-band component of the BL wind is required in the definition of long-lake-axis-parallel (LLAP) bands in Steiger et al. (2013), which are often associated with substantial inland penetration (Veals and Steenburgh 2015).

In this study, we group all variations of shoreline$_{LWK}$ bands within a parent category, which we term *dominant bands*. This choice is motivated both by the common features of the different subcategories and by the observation that bands can evolve between categories (e.g., Peace and Sykes 1966). The dominant band category additionally includes bands with overlake similarities to shoreline$_{LWK}$ bands but inland departures from the quasi-linear arrangement, such as when a band exhibits a bend near landfall, as in Hjelmfelt (1990, his Fig. 1, column II), Byrd et al. (1991, their Fig. 7), or Laird et al. (2003, their Fig. 2b). Finally, the dominant band category includes cases in which one or two bands extend off a lake at an oblique angle to the major lake axis, as in the simulations of Laird et al. (2003; their Figs. 3b,d) or the Type III bands of Niziol et al. (1995) that involve a connection to upstream lakes. Figure 1 shows four examples of dominant bands on NEXRAD reflectivity images and explains the correspondence (or lack thereof) to previous band categorization schemes. We emphasize that the dominant band category is not intended to replace previous, more restrictive band classifications. Rather, *dominant band* is a parent category which encompasses several previous definitions while still removing cases characterized *only* by one or more of nonbanded coverage, cloud streets, and mesovortices. An additional advantage to the judicious use of the dominant band categorization is that it is fully applicable to bodies of water with irregular shapes, such as Lake Superior or Lake Huron, for which it is problematic to unambiguously designate the major lake axis.

Lake-effect snowbands share some common dynamic features (Laird et al. 2003). The presence of a relatively warm body of water below a cold air mass (the fundamental requirement for lake-effect convection) leads to a two-dimensional solenoidal circulation manifested as a quasi-linear band along a third (horizontal) dimension (e.g., Passarelli and Braham 1981; Hjelmfelt and Braham 1983; Bergmaier et al. 2017). This solenoidal circulation is characterized by inflow from one or both sides of the band within the lower portion of the BL (hereafter, lower BL), ascent within the kinematically defined core of the band, and outflow within the upper portion of the BL (hereafter, upper BL; e.g., Peace and Sykes 1966; Baker 1976; Campbell and Steenburgh 2017; Bergmaier et al. 2017). Therefore, environmental thermodynamics and kinematics are important for understanding the properties of lake-effect snowbands.

Several hypotheses have been proposed to explain differences in inland extent among dominant bands. Veals et al. (2018, their Fig. 5b) shows a box-and-whiskers plot for inland penetration (InDist) as a function of CAPE (low, moderate, and high values). The median inland penetration decreased with increasing CAPE, a result they found to be statistically significant at the 95% confidence level. However, Veals et al. discusses a nuanced relationship with instability: during periods of weak flow, higher CAPE favors lesser inland enhancement, whereas during strong flow higher CAPE favors greater inland enhancement. Figure 5 of Villani et al. (2017) shows the correlation coefficient between band length (their term for inland penetration) with a variety of variables, including multiple measures of stability. The correlation is strongly negative with the lake − air temperature difference (i.e., lake T minus air T) at both 850 and 700 mb (1 mb = 1 hPa). Table 3 in Villani et al. (2017) lists the correlation coefficient values as −0.53 and −0.65 for 850 and 700 mb, respectively. It notes that these results are statistically significant at the 99% level. Thus, more unstable environments led to shorter inland penetration here too. An additional hypothesis relates to the impact of vorticity advection on vertical motion in the dominant band in relation to the passage of an upper trough (Campbell et al. 2016). Eipper et al. (2018) explored the statistical relationship between environmental conditions and inland extent, finding differential cold air advection as an important predictor. This finding motivated a closer look at the impact of baroclinity, and its impact in modifying the advective environment, on dominant bands.

In the remainder of the paper, we explore the interaction of dominant bands with environmental baroclinity. The data and methods used in this study are explained in section 2. The research topic is explored in section 3 through an evaluation of environmental baroclinity in lake-effect settings. In section 4, dominant band structures are examined in contrasting cases of weak, strong, and transitioning along-band environmental baroclinity. A discussion is presented in section 5, and conclusions are offered in section 6.

2. Data and methods

To examine the interaction of dominant bands with environmental baroclinity, operational radar images were first inspected to identify time periods from the Ontario Winter Lake-effect Systems (OWLeS; Kristovich et al. 2017) field campaign that featured prolonged occurrences of dominant bands. Specifically, we examined radar images of single or double lake-effect bands that were either isolated or which were estimated to be at least twice as large (in spatial coverage) as any additional lake-effect structures. We employed NEXRAD 4000-ft multiple-radar constant-altitude plan position indicator (CAPPI) images of equivalent radar reflectivity factor (hereafter, reflectivity) obtained from OWLeS archives at UCAR Earth Observing Laboratory (EOL) (http://catalog.eol.ucar.edu/maps/owles). The choice of the 4000-ft level avoided coverage gaps at the 2000-ft level and overshooting at the 6000-ft level (Eipper et al. 2018). Through this preliminary inspection, we identified three favorable time periods for investigation:

1) 0700 UTC 10 December 2013–0000 UTC 14 December 2013,
2) 1300 UTC 6 January 2014–0000 UTC 9 January 2014, and
3) 1300 UTC 27 January 2014–2300 UTC 28 January 2014,

which cover all periods with dominant bands in OWLeS with the exception of the 15–16 December 2013 storm.

Following the identification of these time periods, reanalysis simulations were generated for each period with the Weather Research and Forecasting (WRF) Model (Skamarock et al. 2008). These reanalyses were generated by assimilating hourly in situ observations (e.g., operational surface, aircraft, and radiosonde data were assimilated; radar reflectivities and OWLeS field observations were not assimilated) using the Penn State ensemble Kalman filter data assimilation system (Zhang et al. 2006). WRF was run as a 21-member ensemble using WRF 3.7 with the Advanced Research version of WRF (ARW) dynamical core and 27-, 9-, and 3-km grid spacing nested domains (see Fig. 2); the 3-km domain did not use a cumulus parameterization (Grell and Dévényi 2002). Other model physics choices include the Thompson double-moment microphysics (Thompson et al. 2008), the MYJ boundary layer scheme (Janjić 1994), and the Eta surface layer scheme (Janjić 1996); additional details are described in Saslo and Greybush (2017). This study uses WRF output at 3-km horizontal resolution, unless otherwise noted. Data were interpolated from 43 terrain-following WRF levels to constant pressure levels (with underground data points removed), using a pressure-level spacing of 12.5 hPa between 1050 and 925 hPa, 25 hPa between 925 and 800 hPa, and 50 hPa between 800 and 250 hPa.

An ensemble mean analysis (EMA) was generated for each hour, following the data assimilation step.

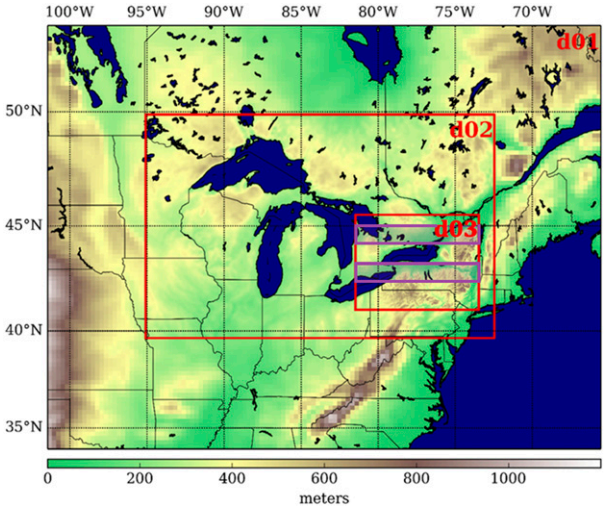

FIG. 2. WRF domains and topography. Domain 1 (d01; 27-km horizontal resolution) comprises the entire map, while domain 2 (d02; 9-km resolution) and domain 3 (d03; 3-km resolution) are indicated by red boxes. The topography displayed within each domain (and outside any nested domain) is the actual terrain field used by WRF in that domain. The two purple-outlined rectangles within domain 3 denote the northern and southern latitudinal averaging windows discussed in section 3.

Advantages of the EMA are that it is generated from the entire ensemble (and therefore averages out random errors associated with individual member perturbations), and that, as an analysis, the EMA is anchored to meteorological observations. However, we did not use the EMA in our case studies due to concerns that the data assimilation and ensemble-averaging steps could result in physical imbalance in the geopotential height/wind fields (e.g., Houtekamer and Mitchell 2001; Greybush et al. 2011; Houtekamer and Zhang 2016) and distortion (i.e., "blurring") of mesoscale kinematic and thermodynamic features.

Instead, we sought a physically balanced and undistorted ensemble member that was mathematically closest to the EMA. This member, designated the "Most Representative ensemble Member" (MRM), was computed through an adaptation of the method used by Lee et al. (2009). The goal in determining the MRM (see the appendix for full details) was to select a single ensemble member that has characteristics most similar (i.e., closest) to a benchmark state (here, the EMA). Closeness to the benchmark state was quantified through normalized mean absolute errors (MAEs) of several key variables considered important to lake-effect processes and morphology: namely, horizontal wind components and temperature at 850 and 700 hPa (e.g., Holroyd 1971; Niziol 1987; Niziol et al. 1995). The 700-hPa level was chosen because it is at or relatively near the capping inversion. In summary, the MRM is designed to avoid unphysical aspects of the EMA but retain EMA strengths. Future mentions of WRF output refer to the MRM, unless otherwise noted.

For the selection of the case studies (presented in section 4), we conducted a preliminary examination of WRF output at each hour within the three reanalysis periods and chose three different cases (i.e., simulation hours) as illustrative examples of the influence of along-band environmental baroclinity on the structure of a dominant band. In one case, the along-band environmental baroclinity is weak, in another it is strong, and in a third it is transitioning between these states. Meanwhile, the cross-band environmental baroclinity is relatively weak and of similar magnitude in all cases. For these case study hours, we compared WRF simulated composite (i.e., column maximum) reflectivity images with NEXRAD 4000-ft CAPPI reflectivity images to verify that WRF was capturing the general north–south placement, east–west extent, and composition of each band.

For both case studies, the synoptic-scale environment was determined primarily from WRF output on the 9- and 3-km domains. Supplemental information was obtained from upper-air charts and soundings from UCAR EOL's OWLeS archives (available online at http://catalog.eol.ucar.edu/owles/ops) and from surface analysis archives from the National Weather Service Weather Prediction Center (available online at http://www.wpc.ncep.noaa.gov/archives/web_pages/sfc/sfc_archive.php).

In addition, vertical–latitudinal cross sections were used to present a detailed view of the band in both case studies. Cross sections provided information about the reflectivity, kinematic, and dynamic structure of the band and its immediate environment. The meridional wind component v captured important features of each band's inflow and outflow, since the orientation of the band at both case-study hours was roughly west to east. Density potential temperature θ_ρ was examined to diagnose the thermodynamic structure of each band and environmental baroclinity. The density potential temperature θ_ρ accounts for the effects of both water vapor and hydrometeors on potential temperature; the formula for its computation is provided in Markowski and Richardson [2010, their Eq. (2.22)]. We chose to position the cross sections over the approximate landfall location and inland portion of each band, where greater human impacts occur. Specifically, the cross sections were generated every 0.5° of longitude (~40–41 km) from 76.21°W (approximately the eastern shore of Lake Ontario) to 74.71°W. Latitudinal bounds of 42.95°

and 44.50°N and a vertical upper bound of 700 hPa were used.

3. Baroclinity in dominant band environments

In this section, we investigate the presence of environmental baroclinity within the three reanalysis periods included in the study. To perform this investigation, we designed metrics to capture the large-scale (i.e., occurring on scales larger than the width of the parent lake) baroclinic environment within which dominant bands existed. Environmental baroclinity revealed by these metrics can include not only synoptic-scale air masses and temperature gradients (e.g., fronts) but also mesoscale air masses (e.g., air masses modified by upwind lakes) and temperature gradients. It was important that both synoptic-scale and mesoscale baroclinity be represented since either one, or both together, can shape the dominant band's environment.

These assessments were performed on the WRF 3-km domain at 950 hPa. We computed them by assessing the *longitudinal variation* (the approximate along-band variation) in both east–west and north–south baroclinity. Longitudinal variation in north–south baroclinity was assessed by subtracting a northern block average of potential temperature θ from a southern block average at each WRF longitude (i.e., every ~3 km) between 73.47° and 81.47°W. The northern and southern averaging windows straddled Lake Ontario and had widths approximately matching that of Lake Ontario; Fig. 2 shows the locations of these windows: 42.3°–43.2°N in the south, and 44.1°–45.0°N in the north. For the assessment of east–west baroclinity, we computed a single latitudinal block average of θ (hereafter $\overline{\theta}$), again at each WRF longitude, and used the entire range of 42.3°–45.0°N as the averaging window. East–west $\overline{\theta}$ variation was then quantified as the difference between the $\overline{\theta}$ value at each longitude and the westernmost $\overline{\theta}$ value.

These baroclinity metrics were corroborated in both qualitative and quantitative ways. We visually compared the results of the metrics to horizontal maps and vertical cross sections and confirmed that the metrics were generally capturing the time-dependent large-scale environment of bands. We experimented with using north/south block minimum θ values rather than block averages, changing the north/south averaging windows to extend one and a half lake-widths from the latitudinal lake center, and using θ_ρ rather than θ; results were very similar. Finally, we assessed baroclinity at 925, 900, and 850 hPa. Results indicated a similar pattern at 925 hPa and a monotonic transition away from the 950-hPa pattern with increasing height, as expected. Since the inflow of lake-effect bands occurs close to the surface and is often very shallow (e.g., Bergmaier et al. 2017), we chose to use 950 hPa in our investigation.

Results of the environmental baroclinity assessments for each reanalysis are presented in Hovmöller diagrams in Fig. 3. Warm colors (positive θ differences) indicate warmer air to the east in Figs. 3a, 3c, and 3e and warmer air to the south in Figs. 3b, 3d, and 3f. Figure 3 reveals that the temperature structure is frequently characterized by warmer air to the south and east, with the former result somewhat more consistent than the latter. Each reanalysis period begins with west–east temperature gradients following an eastward propagating cold front (reflected in the warm colors in the lower-right portions of Figs. 3a, 3c, and 3e); this longitudinal baroclinity is especially strong during the January cases (Figs. 3a,c).

Although the general north–south temperature structure is characterized by warmer air to the south, some notable exceptions occur in the western portion of the domain, most strongly after 1800 UTC 6 January 2014 (Fig. 3d; note the cool colors in the left portion of the image), but also especially between 0000 and 1800 UTC 12 December 2013 (Fig. 3f) and after 0600 UTC 28 January 2014 (Fig. 3b). These features are associated with warm plumes originating over Lake Huron and Georgian Bay. Another exception to the north–south thermal gradient occurs between approximately 1800 UTC 6 January 2014 and 1000 UTC 7 January 2014 (Fig. 3d; note the cool-colored feature which slants upward across the east–west domain). During this time period, a cold mesoscale air mass south of Lake Ontario traversed the region from west to east. This air mass was uniquely cold because it had avoided modification by upwind lakes, similar to a case documented by Campbell and Steenburgh (2017) and Steenburgh and Campbell (2017). In contrast to these thermal-gradient reversals, an especially strong north–south thermal gradient develops after approximately 1200 UTC 13 December 2013 as a cold front approaches and begins to cross the Lake Ontario region from the north (see upper portion of Fig. 3f).

In addition to the baroclinity assessements, Fig. 3 shows the hours when Lake Ontario dominant bands were identified on WRF simulated composite reflectivity (hereafter WRF reflectivity) images. Dominant bands were subjectively identified through inspection of WRF reflectivity in 155 out of 185 total simulation hours (~84%). It is clear from Fig. 3 that environmental baroclinity is frequently present during dominant-band events in all three reanalyses and also exhibits considerable variability in intensity during these events.

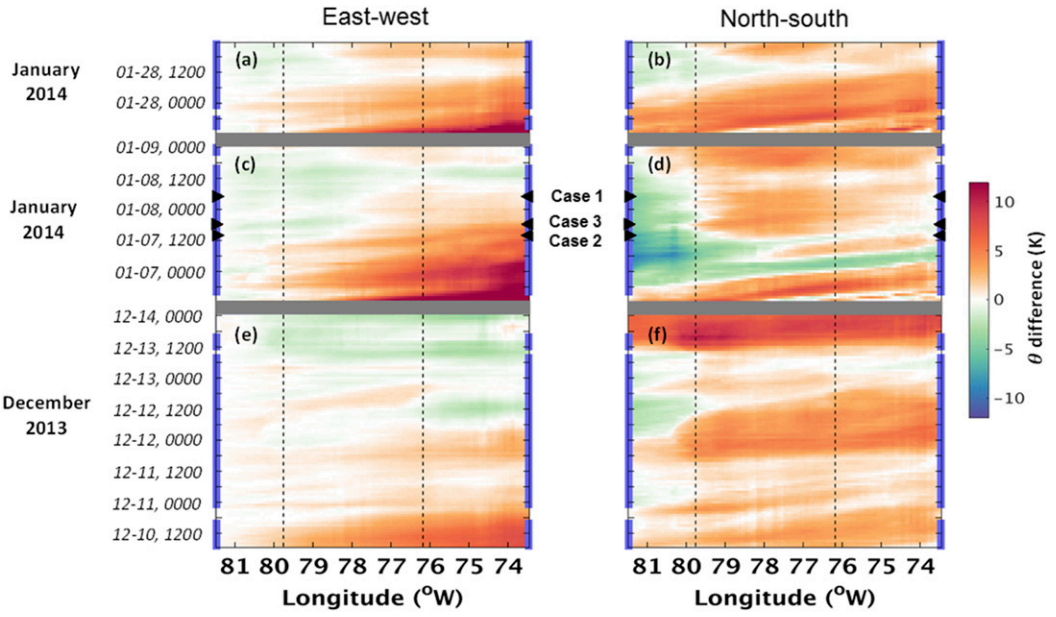

FIG. 3. Hovmöller diagrams of potential temperature θ differences at 950 hPa (K; scale is shown in color bar). (a),(b) The longitudinal variation in east–west and north–south baroclinity, respectively, at each hour from 1300 UTC 27 Jan 2014 to 2300 UTC 28 Jan 2014. Baroclinity is computed using block-averaged θ (see text for computational details). (c),(d) As in (a) and (b), respectively, but at the interval of 1300 UTC 6 Jan 2014–0000 UTC 9 Jan 2014. (e),(f) As in (a) and (b), respectively, but at the interval of 0700 UTC 10 Dec 2013–0000 UTC 14 Dec 2013. Warm colors (positive θ differences) indicate warmer air to the east in (a), (c), and (e) and warmer air to the south in (b), (d), and (f). In each panel, simulation hours are in UTC and increase in the upward direction. The black, dashed vertical lines indicate the approximate east/west ends of Lake Ontario. The thick blue/purple line segments on either side of each panel indicate the hours when dominant bands were identified on WRF simulated composite reflectivity images. The black triangles indicate the hours of the case studies presented in section 4.

Numerous studies have indicated the warm-core nature (i.e., *band-scale* baroclinity) of shoreline$_{LWK}$ bands (including LLAP bands), which results from lake-surface heating and drives a band's mesoscale solenoidal circulation (e.g., Passarelli and Braham 1981; Byrd et al. 1991; Laird et al. 2003; Campbell et al. 2016; Welsh et al. 2016; Bergmaier et al. 2017). In addition, Campbell and Steenburgh (2017) and Steenburgh and Campbell (2017) examined an extended LLAP event on 11 December 2013 and discovered that near-surface air on the southern flank of the LLAP band in the vicinity of the eastern end of Lake Ontario was colder than air on its northern flank. This temperature difference predominantly occurred on a smaller spatial scale than is addressed by our Fig. 3, but nevertheless demonstrates the presence of north–south baroclinity on a scale larger than the width of the band. Our findings extend these results by revealing the prevalence and spatial extent of environmental (or large-scale) baroclinity during three time periods with prolonged dominant band events. Moreover, this environmental baroclinity is not static, but exhibits substantial temporal variability within individual dominant band events. These findings indicate the importance of understanding the spectrum of interactions between dominant bands and varying baroclinic environments. The following section explores this spectrum through several case studies.

4. Case studies

a. *Case 1: Weakly baroclinic (0500 UTC 8 January 2014)*

Case 1 occurred at 0500 UTC 8 January 2014 and was characterized by weak environmental baroclinity compared with the second case study (see Fig. 3). During this time period, an upper-level trough (not shown) traveled eastward across the Lake Ontario region; this trough was exceptionally deep at the onset of the reanalysis period, but gradually broadened and deamplified as it moved eastward. In association with this upper-level trough, a strong cold front traversed the Lake Ontario region on 6 January 2014, ushering in an extended period of west-southwesterly synoptic-scale BL flow. A zone of east–west baroclinity followed the cold front;

this baroclinity was strongest immediately west of the front and gradually weakened farther west. This baroclinic zone is reflected in Fig. 3c from approximately 1300 UTC 6 January 2014 to 1800 UTC 7 January 2014. Following this time interval, the baroclinic zone migrated out of the Lake Ontario region, leaving behind only weak east–west baroclinity for the remainder of the period (Fig. 3c).

Additional information about the environment at 0500 UTC 8 January 2014 is provided in Fig. 4. At 850 hPa, a region of relatively warm air west of Lake Ontario, in combination with the westerly flow, is producing warm air advection (WAA; Fig. 4a). However, the baroclinity and associated WAA are considerably weaker in the central and eastern portions of the domain, where the dominant band is positioned (Figs. 4a,d). At 925 hPa, θ variations are likewise small in the southeastern portion of the domain (Fig. 4b). To the northwest, baroclinity is associated predominantly with 1) warmer, lake-modified plumes associated with Lake Huron/Georgian Bay and Lake Ontario, and 2) a tongue of cooler air positioned along a southwest–northeast axis between Lake Huron (to the northwest) and Lakes Erie and Ontario (to the southeast; Fig. 4b). Near the surface (Fig. 4c), baroclinity is found acrosss the western portions of Lake Ontario (as at 925 hPa), but is weak on the western side of the lake. Figure 4d reveals a west–east-oriented dominant band in the WRF reanalysis originating over west-central Lake Ontario, intensifying over the eastern portion of Lake Ontario, and extending inland over the Tug Hill Plateau and into the Adirondacks. Visual inspection shows that the composition of the band is largely cellular over Lake Ontario with the highest-reflectivity cells (i.e., the band core) arranged in a curvilinear pattern. Inland, the band composition appears less cellular, but a discernable core of higher-reflectivity values penetrates over 40 km from the lake shore. Still farther inland, the band is characterized by a broad area of low reflectivities indicative of stratiform precipitation, similar to the phenomenon documented by Minder et al. (2015). The observed reflectivities (Fig. 4e) also show a dominant band structure at the eastern end of Lake Ontario, extending inland to about 75°W longitude, with the greatest band intensity near 76°W longitude. The band is less visible over the lake in the observed reflectivity compared to the model simulated reflectivity; this can partially be explained by the radar beam overshooting the convection at long distances from the radar located near the Tug Hill Plateau. The bands are comparable in their inland extent, particularly for reflectivity values > 20 dBZ.

Additional insights into the structure of the band are revealed by the vertical–latitudinal cross sections in Fig. 5. Cross section (transect) locations are shown on Fig. 4; we adopt the convention of denoting transects as first, second, third, and fourth with increasing distance eastward (inland). The first reflectivity transect reveals a deep, organized band with low-level maximum reflectivities of around 25 dBZ (Fig. 5a). Collocated with the maximum reflectivities, a pronounced warm plume (with reference to the horizontal surroundings) and strong north–south convergence are present in the lower BL (Figs. 5e,i). The warm plume extends from the surface to around 840 hPa and contains low-level θ_ρ differences of ~3–5 K between the core of the plume and the ambient air (Fig. 5e). North–south convergence is strongest near the surface but extends upward to nearly 850 hPa (Fig. 5i). Directly above this convergent layer, vigorous north–south divergence extends to around 750 hPa. Overall, the first transect (Figs. 5a,e,i) reveals a coherent band structure with maximum reflectivities collocated with positive buoyancy (with repect to the horizontal surroundings) and strong north–south convergence in the lower BL, and with overshooting convection and north–south divergence in the upper BL.

Cross sections from the second, third, and fourth transects reveal a monotonic decrease in maximum reflectivity with distance inland (Figs. 5b–d). Additionally, the band structure widens and its echo-top decreases with distance inland. These reflectivity changes suggest that divergence in the anvil region of the band and hydrometeor fallout are increasingly dominating over the band updraft with distance inland. Analogous to the changes in reflectivity, dynamic and kinematic features of the band progressively decrease in intensity between the first and fourth transects. In the second transect, maximum reflectivities occur at ~43.6°N and are collocated with a pocket of low-level warmer air (Figs. 5b,f); however, this warm pocket is only slightly warmer than its surroundings. In juxtaposition to this weak thermal contrast, appreciable low-level north–south convergence and upper-level north–south divergence are present in the second transect at approximately ~43.7°N (Fig. 5j). Meanwhile, the presence of low-level north–south convergence suggests a Lagrangian pinching off and lofting of the low-level warm plume as it is advected inland, similar to that documented by Campbell and Steenburgh (2017) and Steenburgh and Campbell (2017).

In the third and fourth transects, the low-level warm plume appears to be entirely absent, although a weak north–south θ_ρ gradient persists (Figs. 5g,h). A vertical couplet of weak north–south convergence/divergence is present in the third transect at ~44.1°N, and is again hinted at in the fourth transect (Figs. 5k,l). However, the north–south convergence/divergence are much weaker than in the second transect and are positioned far north of the maximum-reflectivity band core.

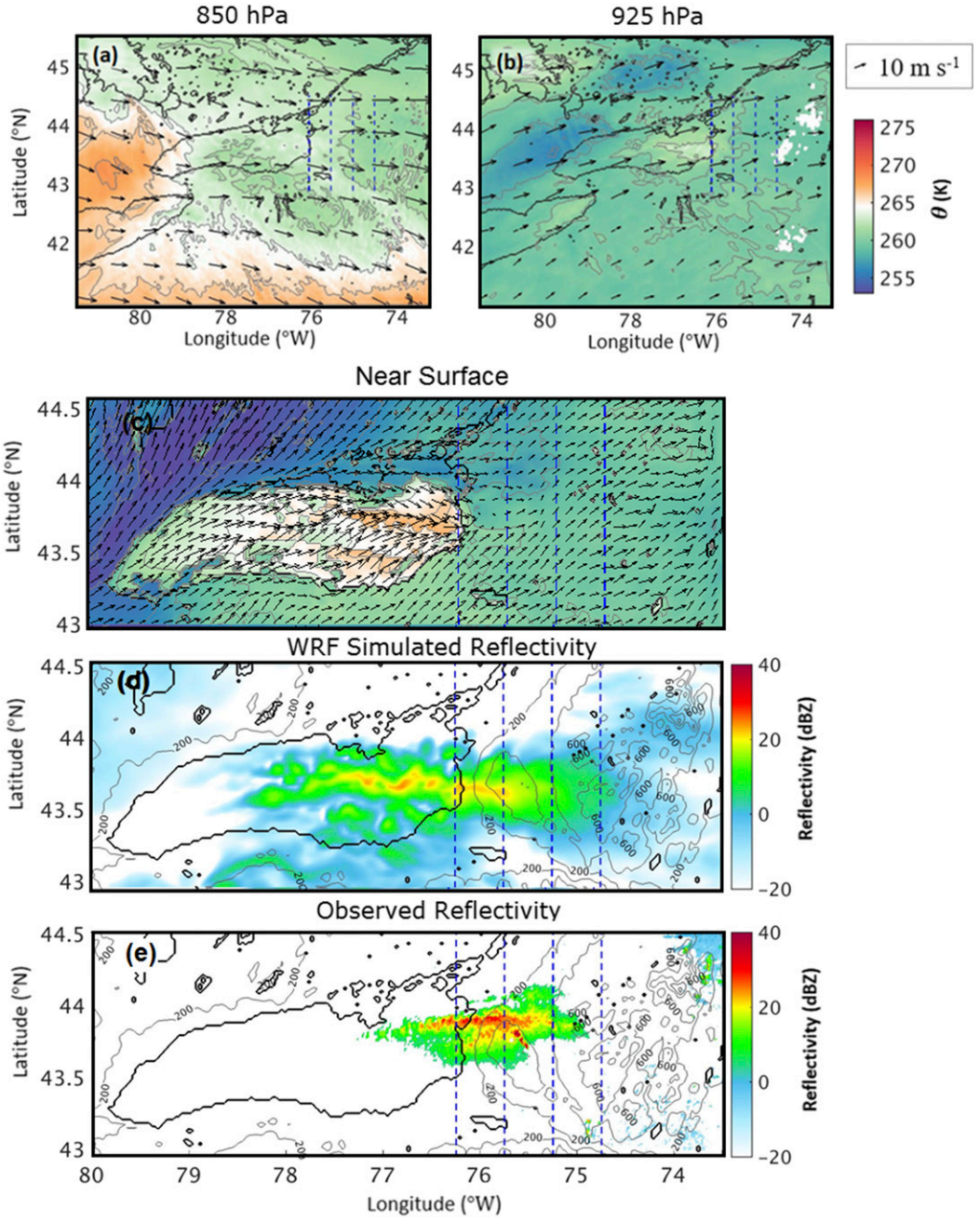

FIG. 4. Meteorological maps at 0500 UTC 8 Jan 2014 (Case 1). (a) WRF 850-hPa potential temperature θ (K; shaded, with color bar to the right of the panels; also contoured in thin gray lines every 2 K) and horizontal wind vectors (a 10 m s^{-1} reference arrow is included to the right of the panels). (b) As in (a), but at 925 hPa [color scale and wind vector scaling are identical to (a)]. White patches in (b) indicate underground locations. (c) As in (a), but showing near-surface variables: potential temperature at 2 m and wind vectors at 10 m; note the reduced domain size in (c). (d) The WRF simulated composite reflectivity (dBZ; shaded, with color bar to the right of the panel) and terrain height [contoured in thin gray lines every 200 m (labeled every 400 m)]. The dashed blue lines in each panel show the locations of the cross sections displayed in Fig. 5 and discussed in the text. (e) The observed composite reflectivity (dBZ), in the same manner as (d).

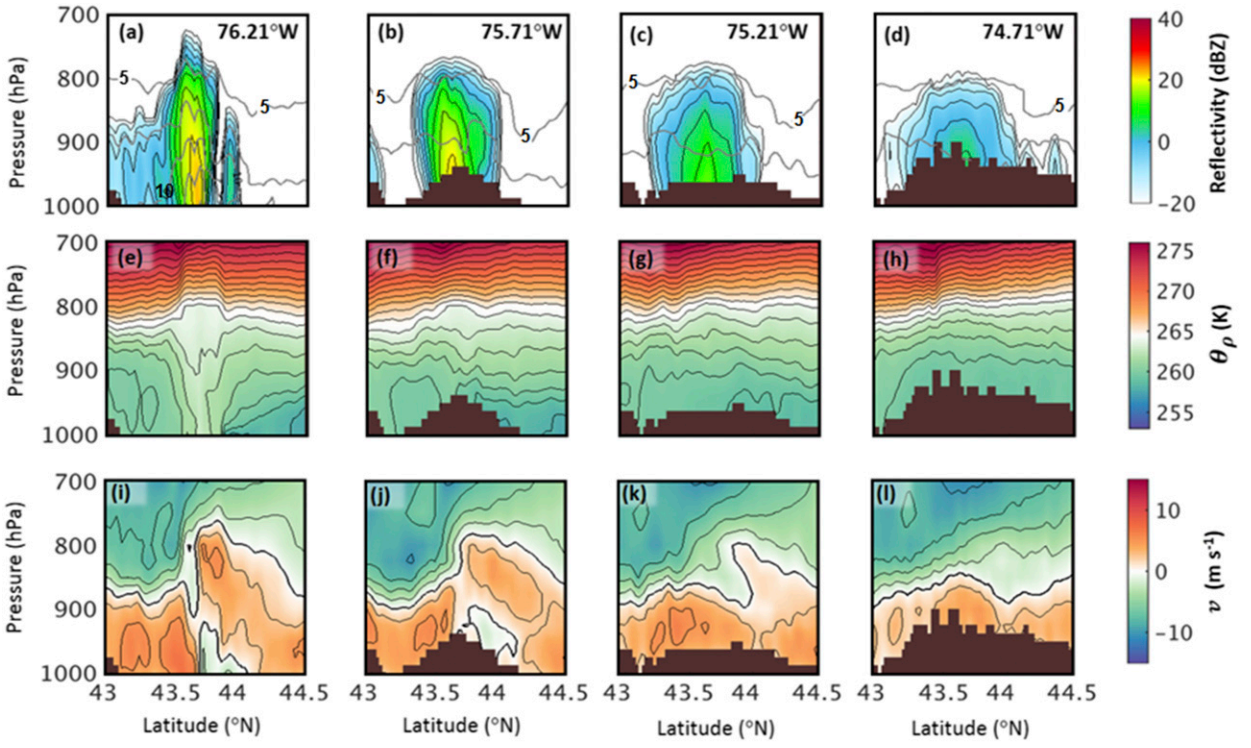

FIG. 5. Vertical–latitudinal WRF cross sections at 0500 UTC 8 Jan 2014 (Case 1). (a)–(d) Simulated reflectivity (dBZ; shaded, with color bar to the right of the panels; also contoured every 5 dBZ) and water vapor mixing ratio (10^{-4} kg kg^{-1}; contoured in gray lines every 2.5×10^{-4} kg kg^{-1}). (e)–(h) Density potential temperature θ_ρ (K; shaded, with color bar to the right of the panels; also contoured every 1 K). (i)–(l) Meridional wind component v (m s^{-1}; shaded, with color bar to the right of the panels; also contoured in thin black lines every 2.5 m s^{-1} with the 0 m s^{-1} contour plotted as a thick black line for emphasis). The longitude listed in the upper-right corner of each reflectivity panel applies to all three cross sections in the corresponding column (cross-section locations are also shown in Fig. 4). Brown indicates underground locations.

A comparison of θ_ρ and v fields across all four transects indicates that the band's mesoscale circulation extends farther inland than its thermodynamic forcing. This pattern suggests a Lagrangian evolution of the band's mesoscale circulation in which the thermal contrast across the band (i.e., the thermal forcing) equilibrates sooner than does the kinematic response, as can be expected from conservation of momentum. Notwithstanding this temporal/spatial lag, the kinematic circulation nevertheless weakens with distance inland so that the band's reflecitivity structure is eventually dominated by upper-BL divergence and hydrometeor fallout.

b. *Case 2: Baroclinic along-band (1400 UTC 7 January 2014)*

Case 2 occurred at 1400 UTC 7 January 2014, 15 h earlier than Case 1,[1] during a period of substantial east–west environmental baroclinity. Figure 3c qualitatively indicates greater east–west baroclinity in Case 2 than in Case 1, and quantitative examination of the data reveals the east–west thermal contrast in Case 2 to be over five times larger than in Case 1. This baroclinity occurred in the wake of an eastward-propagating cold front (see Fig. 3c).

Figure 6a reveals a complex thermal pattern at 850 hPa. The coldest air is located in the south-central portion of the domain while the warmest air is farther east, in association with the synoptic-scale pattern, and to the north, within plumes extending from Georgian Bay and Lake Ontario. An examination of hourly domain 2 maps leading up to Case 2 (not shown) helps to further explain this baroclinic setup. Following the cold frontal passage on 6 January 2014, a deep, cold air mass moved eastward across the Great Lakes region. However, this air mass was dramatically modified by the Great Lakes, leading to substantial intra-airmass mesoscale baroclinity. At 850 hPa, the coldest air became divided into a northen air mass far to the north of Lake Ontario, and a less-extensive air mass just south of Lake Ontario. A similar pattern developed at 925 hPa, but with the coldest air positioned farther west. Also, at 925 hPa,

[1] Despite the chronological sequence, Case 2 is presented second because of its greater baroclinic complexity.

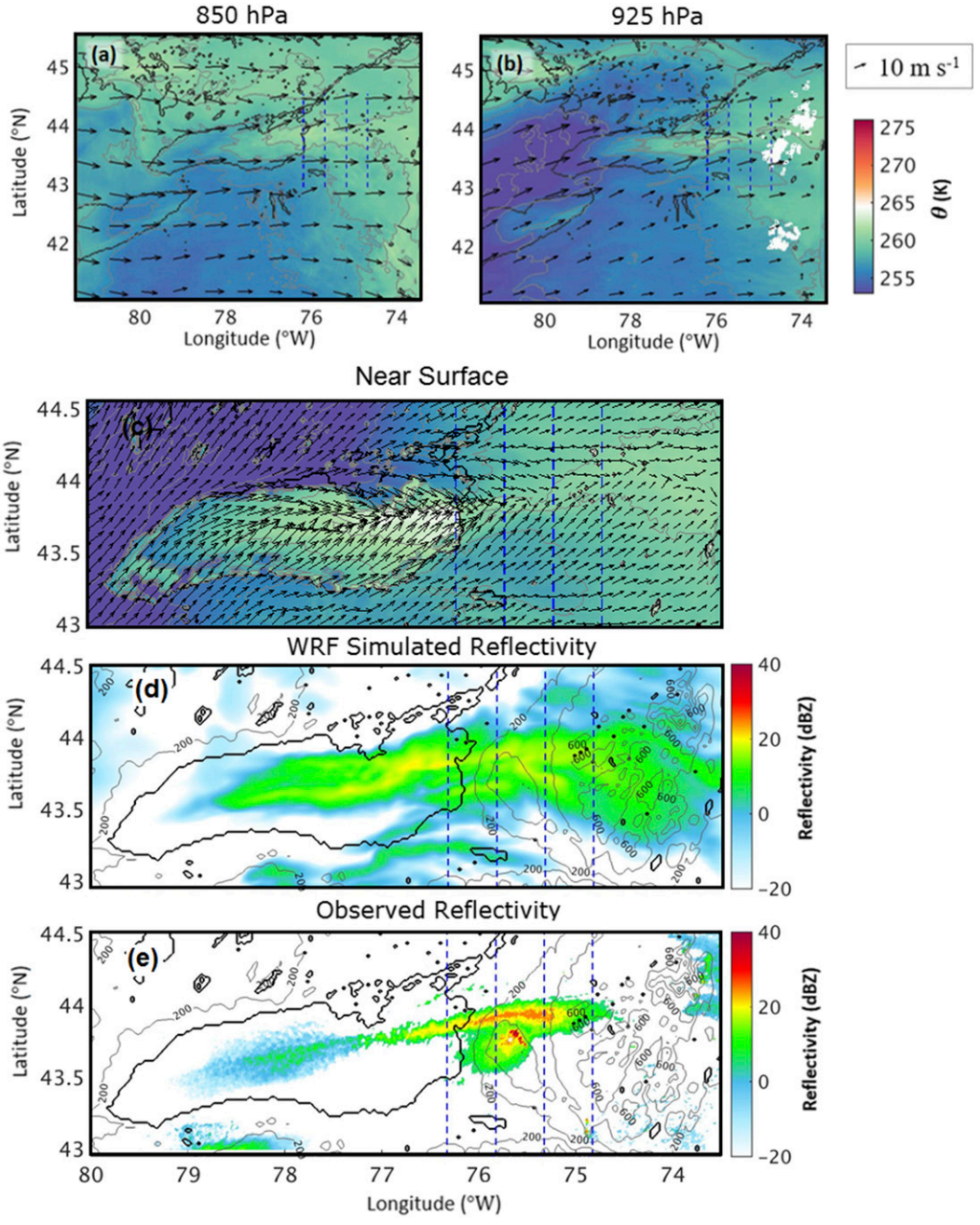

FIG. 6. As in Fig. 4, but at 1400 UTC 7 Jan 2014 (Case 2).

the pocket of very cold air to the south was connected to an additional tongue of exceptionally cold air which had avoided modification by upwind lakes and was positioned between Lake Huron to the north-northwest and Lakes Erie and Ontario to the south-southeast (Fig. 6b). This thermal complexity results in an equally complex pattern of temperature advection. Nevertheless, the *synoptic-scale* temperature gradient is oriented west–east over the southern and central portions of the domain at 925 hPa and over the southeastern portion of the domain at 850 hPa, leading to synoptic-scale CAA at these levels/locations. Cold air advection is also indicated near the surface upwind of Lake Ontario (Fig. 6c).

Case 2, similar to Case 1, features a west–east-oriented dominant band in reflectivity (Fig. 6d; actually the same band documented in Case 1, but 15 h earlier). The band originates over western Lake Ontario, intensifies over central and eastern Lake Ontario and

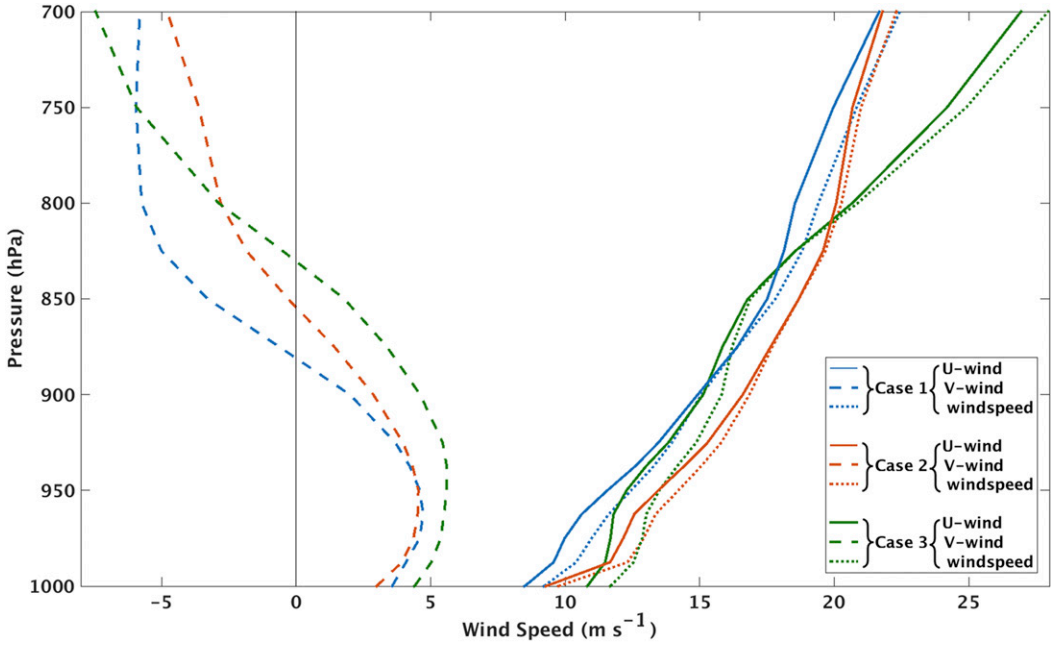

FIG. 7. Vertical profiles of WRF area-averaged longitudinal wind (U-wind), meridional wind (V-wind), and total wind speed (all in m s^{-1}) at both case study hours. Case 1 occurred at 0500 UTC 8 Jan 2014; Case 2 occurred at 1400 UTC 7 Jan 2014; Case 3 occurred at 1800 UTC 7 Jan 2014. See text for details of the area averaging.

extends inland over the northern slope of the Tug Hill Plateau and into the Adirondacks. The model simulated reflectivity structure of the band bears a basic resemblance to the band structure in Case 1 (cf. Figs. 4d and 6d), but a number of differences exist. The maximum reflectivity intensity over eastern Lake Ontario and inland between the first and second transects is lower in Case 2. However, the band originates farther west in Case 2 and the inland penetration of weaker reflectivities (e.g., 10–15 dBZ) is substantially greater in Case 2. Finally, while the reflectivity image reveals a coherent band structure, it also indicates dual reflectivity cores along some portions of the band's length (e.g., between approximately 78.2° and 77°W), as well as weaker additional bands. Examination of the observed reflectivity in Case 2 (Fig. 6e) reveals greater inland extent of the band compared to Case 1 (Fig. 4e), and also some evidence of dual reflectivity cores.

Vertical profiles of area-averaged wind (longitudinal wind, meridional wind, and wind speed) are provided in Fig. 7 for the case studies. Horizontal averaging was performed over the averaging area used in Eipper et al. (2018),[2] which was designed to capture the synoptic-scale environment of lake-effect bands. Examination of Fig. 7 reveals somewhat similar wind profiles in Cases 1 and 2 (and 3), although wind speed in the lower and middle BL is ~1–2 m s^{-1} greater in Case 2 than Case 1. This result is also consistant with Veals et al. (2018) and with Villani et al. (2017), which found that higher wind speeds correspond to greater inland enhancement. Further exploration of the band structure is provided through cross sections.

The first reflectivity crosssection reveals two adjoining reflectivity cores (referred to collectively as the dominant band) located between approximately 43.5° and 44°N, with additional weaker-reflectivity structures to the north and south (Fig. 8a). Of the two adjoining cores, the northern core is deeper and contains higher maximum reflectivities. A strong warm plume is located between these cores and careful inspection reveals that each core is approximately centered on a boundary of the warm plume (Figs. 8a,e). The low-level θ_ρ differences between the warm core and environmental air is ~4–5 K (slightly stronger on the north side). The θ_ρ differences are comparable in magnitude to those in Case 1, but are concentrated in narrower north–south intervals, indicating strong, localized buoyant forcing. Collocated with each reflectivity core are regions of intense lower-BL north–south convergence (extending to ~875–925 hPa) and upper-BL north–south divergence (Fig. 8i). Again, these features are strongest

[2] See their Fig. 2; this averaging rectangle extends ~100 km east and west from Lake Ontario's eastern shoreline and ~25 km inland from both its northern and southern shorelines.

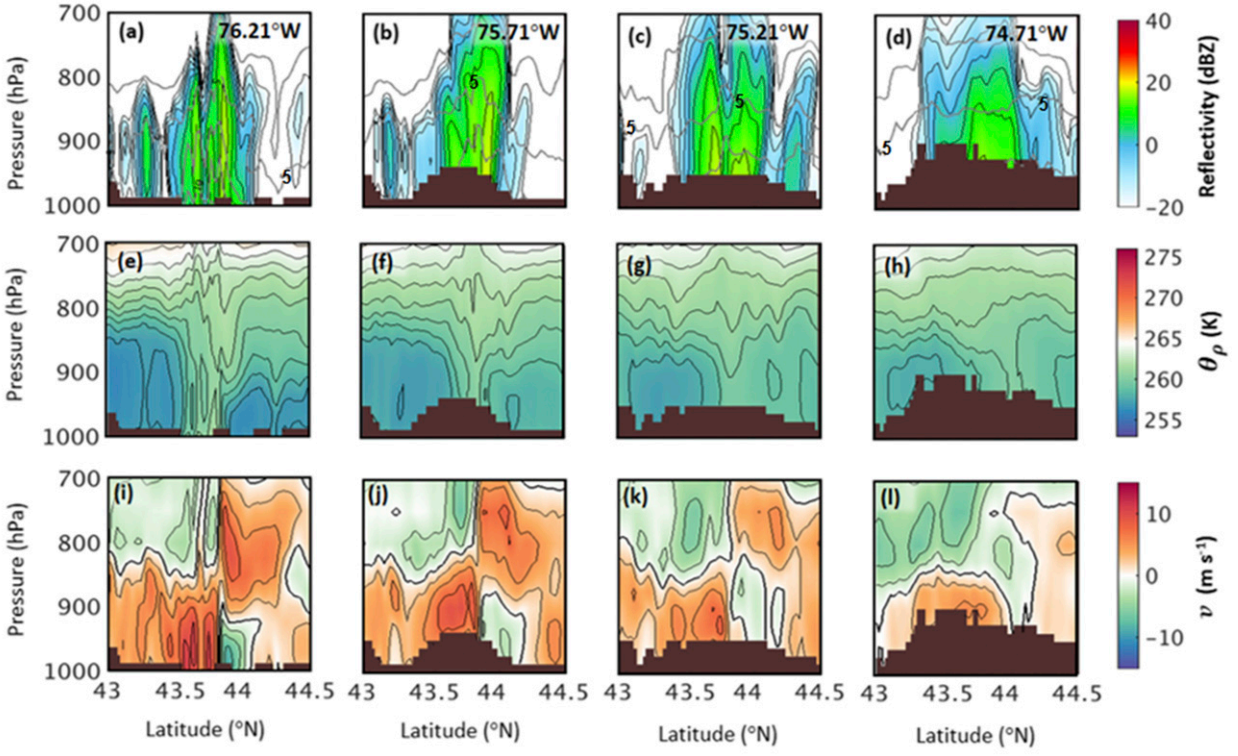

FIG. 8. As in Fig. 5, but at 1400 UTC 7 Jan 2014 (Case 2).

in the northern core where, for instance, near-surface v transitions from 10 to $-7.5\,\mathrm{m\,s^{-1}}$ in ~12 km.

Cross sections from the second, third, and fourth transects reveal a progressive decline in maximum reflectivity with distance inland (Figs. 6c, 8b–d). However, the reduction in maximum reflectivity with distance inland is distinctly more gradual in Case 2 than in Case 1 (cf. Figs. 4c and 5b–d). Another striking difference between the cases is found in the echo top, which demonstrates little to no reduction in height with distance inland in Case 2. Clues to this far-inland maintenance of band intensity and depth are found in the θ_ρ cross sections.

In stark contrast to the near-total pinch-off of the warm plume in the second transect of Case 1, Fig. 8f indicates the continued presence of a pronounced warm plume. Although the isentrope spacing is wider in the second transect than in the first, the thermal contrast remains strong. Moreover, the vertical orientation of the isentropes in the lower BL on the north side of the warm plume indicates a dry-adiabatic atmosphere. Laterally impinging cold air and latent heat release can therefore be expected to produce strong vertical ascent.

In the third transect, the warm plume is substantially weaker and wider, but the isentrope orientation continues to be nearly vertical and even reveals a near-surface layer of static instability (Fig. 8g; note the isentropes slightly tilted over warmer air). The warm plume is also present in the fourth transect and areas of lower-BL static instability exist on both flanks of the band (Fig. 8h). In both the third and fourth transects, lower-BL north–south convergence and upper-BL north–south divergence are approximately collocated with the warmest air (Figs. 8k,l).

c. *Case 3: Transition from baroclinic along-band to weakly baroclinic (1800 UTC 7 January 2014)*

A third case (1800 UTC 7 January 2014), taking place just 4 h after Case 2, illustrates the change in behavior of the lake-effect dominant band structure as a result in changes in along-band environmental baroclinity. At this time, the baroclinity that had been present in Case 2 (Fig. 6b) has weakened considerably (Fig. 9b). This diminution of cold advection is particularly notable along the southern shore of Lake Ontario (Figs. 9b,c). With the change in the thermodynamic environment, the band's inland extent has also changed. The WRF simulated reflectivity now terminates the heaviest precipitation around 75.5°W, indicating a significant reduction in inland extent. The portion of the band that had been advected inland from an earlier time in Case 2 has now faded. The portion of the band generated

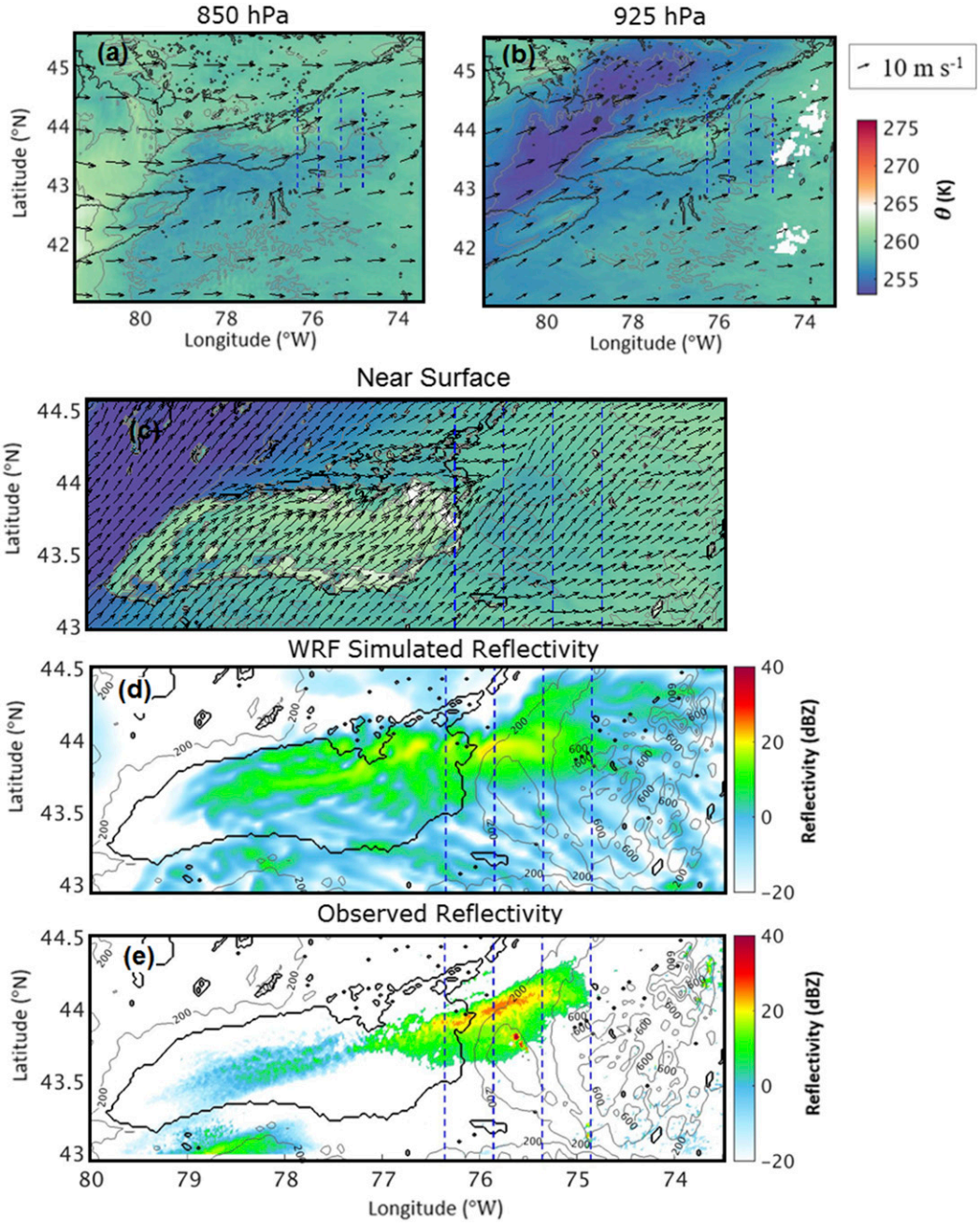

FIG. 9. As in Fig. 4, but at 1800 UTC 7 Jan 2014 (Case 3).

during Case 2, with stronger thermodynamic instability (see potential temperatures in Figs. 4c, 6c, and 9c or middle rows of Figs. 5, 8, and 10) and stronger overturning, has now proceeded inland; with this greater overturning and dissipation, the band pinches off more rapidly and the inland penetration is reduced. Cross sections reveal that an initially strong warm core and overturning circulation in the first transect (Figs. 10a,e) has weakened considerably by the third transect (Figs. 10c,g). The inland structure of the band is now starting to resemble Case 1 rather than Case 2.

5. Discussion

The finding that the Case 2 warm plume penetrates so far inland—apparently *without being lofted from the surface* (Figs. 8e–h)—is surprising in view of the strong north–south convergence (i.e., laterally impinging air)

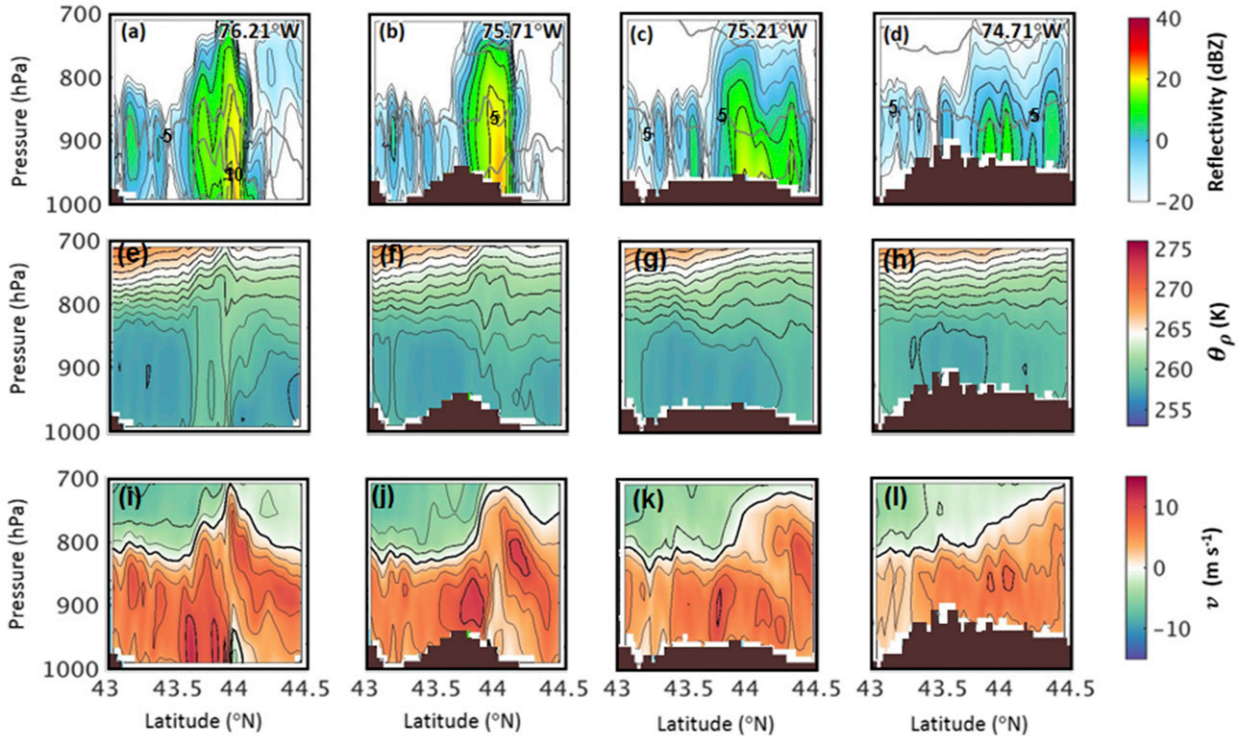

FIG. 10. As in Fig. 5, but at 1800 UTC 7 Jan 2014 (Case 3).

in the lower BL (Figs. 8i–l). In contrast to this structure, the warm plume in Case 1 was almost completely lofted by the second transect and was nearly indistinguishable by the third and fourth transects. The westerly flow in the lower and middle BL is slightly greater in Case 2 than Case 1 (Fig. 7), supporting increased eastward advection of the warm plume. However, the ratio of the inland penetration of the warm plume in Case 2 to that in Case 1 is much greater than the ratio of the zonal wind speed in Case 2 to that in Case 1. Consequently, increased inland advection in Case 2 fails to provide a fully satisfactory explanation for this phenomenon. Villani et al. (2017) and Veals et al. (2018) further explore the relation between low-level wind speed (as well as other factors such as stability/CAPE) and lake-effect snowband characteristics, and it is acknowledged that the atmosphere may have multiple factors acting in concert to affect inland penetration. An additional explanation for the deeply penetrating surface warm plume in Case 2 is related to the complex thermodynamic setup at this time. Figures 6a and 6b shows a warm plume of air extending east from Lake Ontario and merging with a more-extensive region of warm air in the far-eastern portion of the domain. Additional scrutiny of Fig. 6b reveals that the core of *warmest* air extending from Lake Ontario terminates between the second and third transects, *but* that a second and equally warm core originates between the third and fourth transects and broadens toward the east. This thermodynamic structure is schematically represented in Fig. 11b (the thermodynamic structure of Case 1 is schematically represented in Fig. 11a). At the same time, the band's lower-BL environment is coldest in the first transect and is progressively warmer farther east (Figs. 6b and 8e–h), leading to variations in the plume − ambient θ_ρ difference (again refer to Fig. 11b for schematic representation). A listing of the plume − ambient potential temperature differences for the three cases can be found in Table 1.

These variations motivate a brief discussion of density current dynamics, since density currents form along density discontinuities, and are sensitive to the magnitude of the density contrast (e.g., Benjamin 1968; Liu and Moncrieff 1996; note that θ_ρ on an isobaric surface is inversely proportional to density). For a density current, the speed at which more-dense air advances into less-dense air (i.e., the propagation speed of the density current) is proportional to the square root of the θ_ρ difference that exists across the density discontinuity (e.g., Markowski and Richardson 2010). Consequently, for a warm plume with a given value of θ_ρ, colder ambient air (i.e., greater plume − ambient difference) will produce

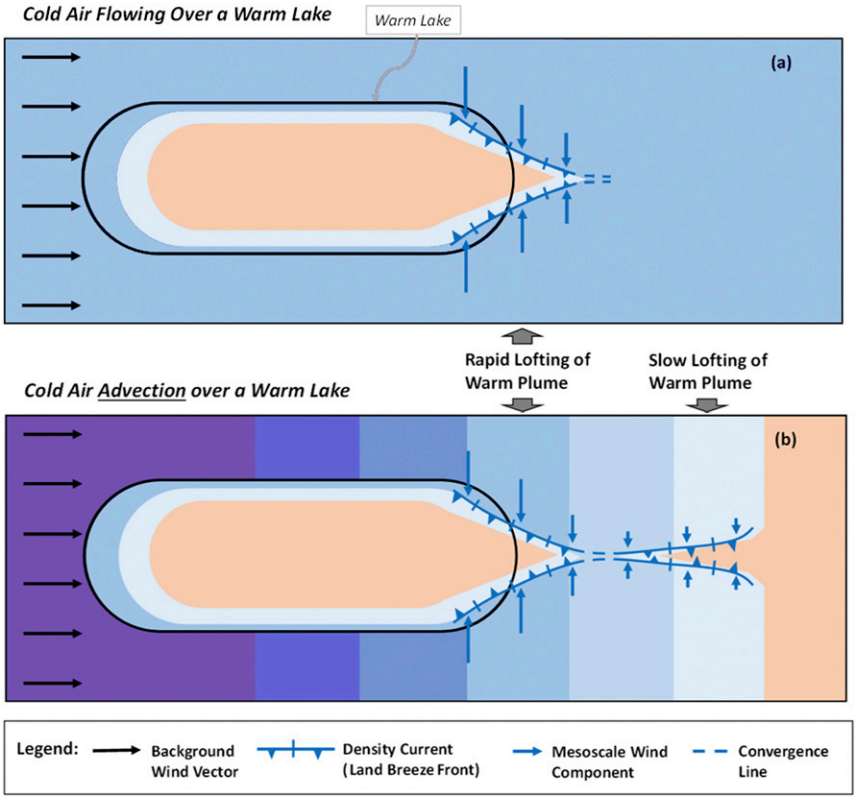

FIG. 11. Conceptual diagram illustrating the hypothesized response of the boundary layer to (a) cold air flowing over a warm lake and (b) cold air *advection* over a warm lake. The dashed blue lines indicate where convergence lines may still be present even though thermal contrast is absent or very weak. Note that in (b), the weaker thermal contrast in the right portion of the figure results in slower lofting of the warm plume, allowing this segment of the warm plume to be advected considerable distances downwind and supporting a long-lived (although more slowly overturning) solenoidal circulation.

faster lateral inflow and more rapid pinch-off/lofting of that plume.

While a comprehensive treatment of density currents in lake-effect settings is beyond the scope of this paper, this discussion suggests an explanation for the thermodynamic structure observed in Case 2 based on the Lagrangian evolution of the band. In the hours preceding the case study hour, the ambient air in the vicinity of Lake Ontario was not as cold and produced a slower pinch-off of the lake-effect warm plume (see the *right* side of Fig. 11b, which represents the environment near Lake Ontario at an earlier time). As this warm plume proceeded to slowly pinch off, it and its environment were being advected eastward by the synoptic-scale wind; this process could be expected to eventually result in the thermodynamic structure observed in Figs. 8g and 8h and the eastern portion of Fig. 6b and schematically represented in Fig. 11b in the region denoted with the text "Slow Lofting of Warm Plume." In contrast, in the time immediately preceding and including Case 2, the colder ambient air was producing a more rapid pinch-off, leading to reduced (Lagrangian) inland penetration of this segment of the warm plume (schematically represented in Fig. 11b in the region denoted with the text "Rapid Lofting of Warm Plume"). In the mechanism outlined above, the strong along-band baroclinic setting of Case 2 allows both band responses to exist simultaneously at different locations along the

TABLE 1. Plume − ambient differences in potential temperature (K) at 2 m above the surface calculated for each of three cases (see Fig. 3) and each of four transects along a meridian of longitude (see Fig. 4; moving from west to east). The plume − ambient difference was calculated as the average of the differences from the plume (identified as a local maximum in potential temperature along the transect) to the ambient air to its north and to its south.

Transect	1	2	3	4
Case 1	7.2	2.3	—	—
Case 2	7.1	2.8	1.8	2
Case 3	5.9	1.2	1.1	—

band, and also allows the spatial transition between these responses. In contrast, Case 1—with much weaker east–west baroclinity—is characterized only by moderately rapid lofting of the warm plume (schematically represented in Fig. 11a). Despite having a somewhat weaker overturning circulation at the lake shore in steady state, the band in Case 1 does not extend inland as far as Case 2, because the latter case benefits from the even slower lofting of the warm plume from several hours previous being advected toward the east. Ultimately, this discussion indicates that the unique baroclinic arrangement in Case 2 may be responsible for the large inland penetration of the warm plume and the band. Note, however, that the very conditions which favor inland penetration, slower solenoidal overturning of the band, also leads to a weaker band. For sufficiently weak bands, other mechanisms for band decay (drag for example) may become the limiting factor in inland penetration. Thus, if lake-induced instability is too limited inland penetration would also decrease. The optimum should, therefore, be reached not immediately after cold frontal passage, when cold advection is typically strongest, but somewhat later when the air mass has become significantly colder than the lake surface. The idealized schematic diagrams in Fig. 11 can be compared to the modeled near-surface temperature and wind fields in Figs. 4c, 6c, and 9c; note in particular how the warm plume pinches off then broadens again in Fig. 6c, which is in agreement with Fig. 11b.

To summarize, looking at this work and Eipper et al. (2018), we see two mechanisms relating inland penetration to along-band cold advection. Eipper et al. (2018) discussed the role of differential temperature advection in creating CAPE downwind of the lake for sustained band convection. This work discusses an additional potential mechanism whereby a ''sweet spot'' is achieved between the slowing of the solenoidal circulation destroying its own warm core (for smaller air–land temperature differences) and dissipative factors including surface friction and internal mixing, which would particularly destroy weaker solenoidal circulations resulting from weak land–lake temperature differences.

6. Conclusions

An examination of baroclinity (presented in section 3) indicates that Lake Ontario dominant bands frequently form or persist in the presence of both weak and strong environmental baroclinity. During the three reanalysis periods studied, varying degrees of baroclinity were commonly observed at a scale larger than the width of Lake Ontario (Fig. 3). In addition, this research indicates that sources of this environmental baroclinity may be divided into two main categories:

1) synoptic-scale weather features, such as cold fronts and surface troughs, and
2) mesoscale features, frequently produced through airmass modification by upwind Great Lakes, including warm plumes extending off of Lake Huron/Georgian Bay. Also included in this category are cases in which a mesoscale air mass crosses a landbridge and escapes modification by upwind lakes, leaving it colder than modified air on either side of it.

Multiple scales of baroclinity (e.g., synoptic-scale, mesoscale, band-scale) were often present simultaneously within the reanalyses, leading to a complex thermal environment. This complexity is likely to be especially great for Lake Ontario because its geographic position causes it to be frequently downwind of other Great Lakes; variations in baroclinity can often be attributed to modification by upwind lakes.

The case studies in section 4 provide insight into the spectrum of possible interactions between dominant bands and environmental baroclinity. The two contrasting cases exhibit striking differences in the inland structure of the dominant band. In Case 1, in a weakly baroclinic environment, the band structure indicates rapid thermodynamic equilibration and corresponding small inland penetration (since kinematic equilibration follows soon after dynamic equilibration). In contrast, the band structure in Case 2 exhibits strong, deep thermodynamic forcing for the band more than 120 km inland from Lake Ontario. Our hypothesis for the inland persistence of thermodynamic forcing in Case 2 is that the strong along-band baroclinity is resulting in slower solenoidal overturning of the warm plume in the eastern portion of the band. Case 3 reveals a transition from strongly baroclinic to weakly baroclinic, with a corresponding reduction in inland penetration.

This study offers additional perspective on the importance synoptic-scale vertically differential cold air advection (CAA) in the inland penetration of LLAP. While the results of Eipper et al. (2018) have not yet been fully generalized, we note that synoptic-scale CAA within the BL was present during Case 2. Notwithstanding this, the thermodynamic and kinematic features of the band and the BL in Case 2 suggest that near-surface baroclinic zones/boundaries strongly influence the development and inland penetration of the dominant band. The Case 2 analysis also suggests that CAA could have an important influence on dominant band inland penetration even when the CAA is not necessarily vertically differential. Thus, it is possible that Eipper et al. (2018) captures *one* process that impacts dominant bands

during periods of cold air advection, but that additional processes are important as well.

Overall, these results indicate that environmental baroclinity plays an important role in shaping the inland structure and characteristics of dominant bands, including LLAP bands. We recommend that future studies synthesize the results of this and previous studies and continue to explore the prevalance and characteristics of environmental baroclinity over longer observation periods and for other bodies of water. We also encourage future investigations to continue to examine the structure and behavior of dominant bands in the presence of environmental baroclinity of varying orientation and intensity, so that this knowledge can potentially result in more accurate operational weather forecasts of intense lake-effect bands, with accompianing socioeconomic benefits.

Acknowledgments. We gratefully acknowledge the entire team of OWLeS scientists and students for their dedicated field work under challenging conditions. We thank Sue Ellen Haupt, Jared Lee, and Yvette Richardson, and three anonymous reviewers, for helpful discussions that improved the quality of this research. Some computations for this research were performed on the Pennsylvania State University's Institute for CyberScience Advanced CyberInfrastructure (ICS-ACI). Special thanks is extended to the EOL of NCAR for maintaining the OWLeS data repository. This work was funded by the National Science Foundation Grants AGS-1259011 (D. E. and G. Y.), AGS-1259020 (T. S. and R. C.), and AGS-1745243 (S. G. and S. S.).

APPENDIX

Most Representative Ensemble Member (MRM) Determination

The methodology for determining the Most Representative ensemble Member (MRM) is an adaptation of a method used in Lee et al. (2009, p. 2310). We begin by identifying the benchmark state the MRM is designed to represent. While observations are clearly a valid option for this benchmark state, we choose instead to use the ensemble mean analysis (EMA), which is closely linked to observations through EnKF data assimilation but has the advantage of a much higher spatial resolution (3-km grid spacing) and full dynamical fields. We then designate variables of interest (including sampling levels), choosing, in our case, to use horizontal wind components and temperature at 700 and 850 hPa.

Following these design choices, we use normalized mean absolute errors (MAEs) to determine the ensemble member mathematically closest to the benchmark state. We first compute the MAE (e.g., Wilks 2006) for each ensemble member and variable of interest, obtaining individual values of $\mathrm{MAE}^m_{\mathrm{var}}$, where m is the ensemble member and var is the variable of interest. The $\mathrm{MAE}^m_{\mathrm{var}}$ values are then normalized by dividing by $\overline{\mathrm{MAE}}_{\mathrm{var}}$, the mean MAE for that variable computed across all ensemble members. The sum of the normalized MAEs for a particular member m is given by

$$\mathrm{sum}^m = \sum_{\text{all vars}} \left(\frac{\mathrm{MAE}^m_{\mathrm{var}}}{\overline{\mathrm{MAE}}_{\mathrm{var}}} \right), \tag{A1}$$

where $\sum_{\text{all vars}}()$ refers to summation across all variables of interest. The ensemble member that minimizes sum^m is mathematically closest to the benchmark state (by this method) and is designated the MRM.

REFERENCES

Baker, D. G., 1976: The mesoscale temperature and dew point fields of a very cold airflow across the Great Lakes. *Mon. Wea. Rev.*, **104**, 860–867, https://doi.org/10.1175/1520-0493(1976)104<0860:TMTADP>2.0.CO;2.

Ballentine, R. J., 1982: Numerical simulation of land-breeze-induced snowbands along the western shore of Lake Michigan. *Mon. Wea. Rev.*, **110**, 1544–1553, https://doi.org/10.1175/1520-0493(1982)110<1544:NSOLBI>2.0.CO;2.

Benjamin, T. B., 1968: Gravity currents and related phenomena. *J. Fluid Mech.*, **31**, 209–248, https://doi.org/10.1017/S0022112068000133.

Bergmaier, P. T., B. Geerts, L. S. Campbell, and W. J. Steenburgh, 2017: The OWLeS IOP2b lake-effect snowstorm: Dynamics of the secondary circulation. *Mon. Wea. Rev.*, **145**, 2437–2459, https://doi.org/10.1175/MWR-D-16-0462.1.

Byrd, G. P., R. A. Anstett, J. E. Heim, and D. M. Usinski, 1991: Mobile sounding observations of lake-effect snowbands in western and central New York. *Mon. Wea. Rev.*, **119**, 2323–2332, https://doi.org/10.1175/1520-0493(1991)119<2323:MSOOLE>2.0.CO;2.

Campbell, L. S., and W. J. Steenburgh, 2017: The OWLeS IOP2b lake-effect snowstorm: Mechanisms contributing to the Tug Hill precipitation maximum. *Mon. Wea. Rev.*, **145**, 2461–2478, https://doi.org/10.1175/MWR-D-16-0461.1.

——, ——, P. G. Veals, T. W. Letcher, and J. R. Minder, 2016: Lake-effect mode and precipitation enhancement over the Tug Hill Plateau during OWLeS IOP2b. *Mon. Wea. Rev.*, **144**, 1729–1748, https://doi.org/10.1175/MWR-D-15-0412.1.

Eipper, D. T., G. S. Young, S. J. Greybush, S. Saslo, T. D. Sikora, and R. D. Clark, 2018: Predicting the inland penetration of long-lake-axis-parallel snowbands. *Wea. Forecasting*, **33**, 1435–1451, https://doi.org/10.1175/WAF-D-18-0033.1.

Grell, G. A., and D. Dévényi, 2002: A generalized approach to parameterizing convection combining ensemble and data assimilation techniques. *Geophys. Res. Lett.*, **20**, 1693, https://doi.org/10.1029/2002GL015311.

Greybush, S. J., E. Kalnay, T. Miyoshi, K. Ide, and B. R. Hunt, 2011: Balance and ensemble Kalman filter localization techniques. *Mon. Wea. Rev.*, **139**, 511–522, https://doi.org/10.1175/2010MWR3328.1.

Hjelmfelt, M. R., 1990: Numerical study of the influence of environmental conditions on lake-effect snowstorms over Lake Michigan. *Mon. Wea. Rev.*, **118**, 138–150, https://doi.org/10.1175/1520-0493(1990)118<0138:NSOTIO>2.0.CO;2.

——, and R. R. Braham, 1983: Numerical simulation of the airflow over Lake Michigan for a major lake-effect snow event. *Mon. Wea. Rev.*, **111**, 205–219, https://doi.org/10.1175/1520-0493(1983)111<0205:NSOTAO>2.0.CO;2.

Holroyd, E. W., III, 1971: Lake-effect cloud bands as seen from weather satellites. *J. Atmos. Sci.*, **28**, 1165–1170, https://doi.org/10.1175/1520-0469(1971)028<1165:LECBAS>2.0.CO;2.

Houtekamer, P. L., and H. L. Mitchell, 2001: A sequential ensemble Kalman filter for atmospheric data assimilation. *Mon. Wea. Rev.*, **129**, 123–137, https://doi.org/10.1175/1520-0493(2001)129<0123:ASEKFF>2.0.CO;2.

——, and F. Zhang, 2016: Review of the ensemble Kalman filter for atmospheric data assimilation. *Mon. Wea. Rev.*, **144**, 4489–4532, https://doi.org/10.1175/MWR-D-15-0440.1.

Janjić, Z. I., 1994: The step-mountain eta coordinate model: Further developments of the convection, viscous sublayer, and turbulence closure schemes. *Mon. Wea. Rev.*, **122**, 927–945, https://doi.org/10.1175/1520-0493(1994)122<0927:TSMECM>2.0.CO;2.

——, 1996: The surface layer in the NCEP Eta Model. Preprints, *11th Conf. on Numerical Weather Prediction*, Norfolk, VA, Amer. Meteor. Soc., 354–355.

Jiusto, J. E., and M. L. Kaplan, 1972: Snowfall from lake-effect storms. *Mon. Wea. Rev.*, **100**, 62–66, https://doi.org/10.1175/1520-0493(1972)100<0062:SFLS>2.3.CO;2.

Kelly, R. D., 1986: Mesoscale frequencies and seasonal snowfalls for different types of Lake Michigan snow storms. *J. Climate Appl. Meteor.*, **25**, 308–312, https://doi.org/10.1175/1520-0450(1986)025<0308:MFASSF>2.0.CO;2.

Kristovich, D. A. R., and R. A. Steve III, 1995: A satellite study of cloud-band frequencies over the Great Lakes. *J. Appl. Meteor.*, **34**, 2083–2090, https://doi.org/10.1175/1520-0450(1995)034<2083:ASSOCB>2.0.CO;2.

Kristovich, D., and Coauthors, 2017: The Ontario Winter Lake-Effect Systems Field Campaign: Scientific and educational adventures to further our knowledge and prediction of lake-effect storms. *Bull. Amer. Meteor. Soc.*, **98**, 315–332, https://doi.org/10.1175/BAMS-D-15-00034.1.

Laird, N. F., J. E. Walsh, and D. A. R. Kristovich, 2003: Model simulations examining the relationship of lake-effect morphology to lake shape, wind direction, and wind speed. *Mon. Wea. Rev.*, **131**, 2102–2111, https://doi.org/10.1175/1520-0493(2003)131<2102:MSETRO>2.0.CO;2.

Lee, J. A., L. J. Peltier, S. E. Haupt, J. C. Wyngaard, D. R. Stauffer, and A. Deng, 2009: Improving SCIPUFF dispersion forecasts with NWP ensembles. *J. Appl. Meteor. Climatol.*, **48**, 2305–2319, https://doi.org/10.1175/2009JAMC2171.1.

Liu, C. H., and M. W. Moncrieff, 1996: A numerical study of the effects of ambient flow and shear on density currents. *Mon. Wea. Rev.*, **124**, 2282–2303, https://doi.org/10.1175/1520-0493(1996)124<2282:ANSOTE>2.0.CO;2.

Markowski, P., and Y. Richardson, 2010: *Mesoscale Meteorology in Midlatitudes*. Wiley-Blackwell, 430 pp.

Minder, J. R., T. W. Letcher, L. S. Campbell, P. G. Veals, and W. J. Steenburgh, 2015: The evolution of lake-effect convection during landfall and orographic uplift as observed by profiling radars. *Mon. Wea. Rev.*, **143**, 4422–4442, https://doi.org/10.1175/MWR-D-15-0117.1.

Niziol, T. A., 1987: Operational forecasting of lake-effect snowfall in western and central New York. *Wea. Forecasting*, **2**, 310–321, https://doi.org/10.1175/1520-0434(1987)002<0310:OFOLES>2.0.CO;2.

——, W. R. Snyder, and J. S. Waldstreicher, 1995: Winter weather forecasting throughout the eastern United States. Part IV: Lake effect snow. *Wea. Forecasting*, **10**, 61–77, https://doi.org/10.1175/1520-0434(1995)010<0061:WWFTTE>2.0.CO;2.

Passarelli, R. E., Jr., and R. R. Braham Jr., 1981: The role of the winter land breeze in the formation of Great Lake snow storms. *Bull. Amer. Meteor. Soc.*, **62**, 482–491, https://doi.org/10.1175/1520-0477(1981)062<0482:TROTWL>2.0.CO;2.

Peace, R. L., and R. B. Sykes, 1966: Mesoscale study of a lake-effect snowstorm. *Mon. Wea. Rev.*, **94**, 495–507, https://doi.org/10.1175/1520-0493(1966)094<0495:MSOALE>2.3.CO;2.

Saslo, S., and S. J. Greybush, 2017: Prediction of lake-effect snow using convection-allowing ensemble forecasts and regional data assimilation. *Wea. Forecasting*, **32**, 1727–1744, https://doi.org/10.1175/WAF-D-16-0206.1.

Sikora, T. D., G. S. Young, E. O'Marr, and R. F. Garparovic, 2001: Anomalous cloud lines over the mid-Atlantic coast of the United States. *Can. J. Remote Sens.*, **27**, 320–327, https://doi.org/10.1080/07038992.2001.10854874.

Skamarock, W. C., and Coauthors, 2008: A description of the Advanced Research WRF version 3. NCAR Tech. Note NCAR/TN-475+STR, 113 pp., https://doi.org/10.5065/D68S4MVH.

Steenburgh, W. J., and L. S. Campbell, 2017: The OWLeS IOP2b lake-effect snowstorm: Shoreline geometry and the mesoscale forcing of precipitation. *Mon. Wea. Rev.*, **145**, 2421–2436, https://doi.org/10.1175/MWR-D-16-0460.1.

Steiger, S. M., and Coauthors, 2013: Circulations, bounded weak echo regions, and horizontal vortices observed within long-lake-axis-parallel–lake-effect storms by the Doppler on Wheels. *Mon. Wea. Rev.*, **141**, 2821–2840, https://doi.org/10.1175/MWR-D-12-00226.1.

Thompson, G., P. R. Field, R. M. Rasmussen, and W. D. Hall, 2008: Explicit forecasts of winter precipitation using an improved bulk microphysics scheme. Part II: Implementation of a new snow parameterization. *Mon. Wea. Rev.*, **136**, 5095–5115, https://doi.org/10.1175/2008MWR2387.1.

Veals, P. G., and W. J. Steenburgh, 2015: Climatological characteristics and orographic enhancement of lake-effect precipitation east of Lake Ontario and over the Tug Hill Plateau. *Mon. Wea. Rev.*, **143**, 3591–3609, https://doi.org/10.1175/MWR-D-15-0009.1.

——, ——, and L. S. Campbell, 2018: Factors affecting the inland and orographic enhancement of lake-effect precipitation over the Tug Hill Plateau. *Mon. Wea. Rev.*, **146**, 1745–1762, https://doi.org/10.1175/MWR-D-17-0385.1.

Villani, J. P., M. L. Jurewicz Sr., and K. Reinhold, 2017: Forecasting the inland extent of lake effect snow bands downwind of Lake Ontario. *J. Oper. Meteor.*, **5**, 53–70, https://doi.org/10.15191/nwajom.2017.0505.

Welsh, D., B. Geerts, J. Minder, J. Steenburgh, P. Bergmaier, X. Jing, and L. Campbell, 2016: Understanding heavy lake-effect snowfall: the vertical structure of radar reflectivity in a deep snowband over and downwind of Lake Ontario. *Mon. Wea. Rev.*, **144**, 4221–4244, https://doi.org/10.1175/MWR-D-16-0057.1.

Wilks, D. S., 2006: *Statistical Methods in the Atmospheric Sciences*. 2nd ed. International Geophysics Series, Vol. 100, Academic Press, 648 pp.

Zhang, F., Z. Meng, and A. Aksoy, 2006: Tests of an ensemble Kalman filter for mesoscale and regional-scale data assimilation. Part I: Perfect model experiments. *Mon. Wea. Rev.*, **134**, 722–736, https://doi.org/10.1175/MWR3101.1.